**Article:**
Lehmeier, C., Pajor, R., Lundgren, M.R. et al. (13 more authors) (2017) Cell density and airspace patterning in the leaf can be manipulated to increase leaf photosynthetic capacity. Plant Journal . ISSN 0960-7412

https://doi.org/10.1111/tpj.13727

Article Type: Original Article

# Cell density and airspace patterning in the leaf can be manipulated to increase leaf photosynthetic capacity

Christoph Lehmeier[1,5,§], Radoslaw Pajor[2,§], Marjorie R. Lundgren[1,§], Andrew Mathers[2], Jen Sloan[1], Marion Bauch[1], Alice Mitchell[1], Chandra Bellasio[1,8], Adam Green[3], Daniel Bouyer[4,6], Arp Schnittger[4,7], Craig Sturrock[2], Colin P. Osborne[1], Stephen Rolfe[1], Sacha Mooney[2], Andrew J. Fleming[1,*]

[1]Department of Animal and Plant Sciences, University of Sheffield, Western Bank, Sheffield S10 2TN, UK

[2]Division of Agriculture and Environmental Sciences, School of Biosciences, University of Nottingham, Sutton Bonington Campus, Loughborough LE12 5RD, UK

[3]Department of Physics and Astronomy, University of Sheffield, Hounsfield Road, Sheffield S3 7RH, UK

[4]Institut de Biologie Moleculaire des Plantes du CNRS, IBMP-CNRS-UPR2357, 12, rue du General Zimmer, 67084 Strasbourg, France

[§]contributed equally to this paper

Current address:

[5]Department of Ecology and Evolutionary Biology, Kansas Biological Survey, The University of Kansas, 2101 Constant Ave., Lawrence, KS 66047, USA

[6]Institut de Biologie de l'ENS, UMR8197 - INSERM U1024, Ecole Normale Supérieure, 46 rue d'Ulm, 75230 Paris cedex 05, France

[7]University of Hamburg, Biozentrum Klein Flottbek, Department of Developmental Biology, Ohnhorststr. 18 - 22609 Hamburg, Germany

This article has been accepted for publication and undergone full peer review but has not been through the copyediting, typesetting, pagination and proofreading process, which may lead to differences between this version and the Version of Record. Please cite this article as doi: 10.1111/tpj.13727

[8] Research School of Biology, Australian National University, Acton, ACT, 2601 Australia.

*Corresponding author: a.fleming@sheffield.ac.uk

**Running Title:** Leaf cellular anatomy and photosynthesis

**Key Words:** leaf, Cell division, photosynthesis, *Arabidopsis thaliana*, differentiation

**ABSTRACT**

**The pattern of cell division, growth and separation during leaf development determines the pattern and amount of airspace in a leaf. The resulting balance of cellular material and airspace is expected to significantly influence the primary function of the leaf, photosynthesis, yet the manner and degree to which cell division patterns impact airspace networks and photosynthesis remains largely unexplored. In this paper we investigate the relationship of cell size and patterning, airspace and photosynthesis by promoting and repressing the expression of cell cycle genes in the leaf mesophyll. Using microCT imaging to quantify leaf cellular architecture and fluorescence/gas exchange analysis to measure leaf function, we show that increased cell density in the mesophyll of Arabidopsis can be used to increase leaf photosynthetic capacity. Our analysis suggests this occurs both by increasing tissue density (decreasing the relative amount of airspace) and by altering the pattern of airspace distribution within the leaf. Our results indicate that cell division patterns influence the photosynthetic performance of a leaf and that it is possible to engineer improved photosynthesis via this approach.**

## INTRODUCTION

The internal architecture of a leaf arises by a combined process of cell growth and division, coupled to regulated cell separation events that determine the pattern and extent of airspace formed in particular regions of the leaf. This pattern of airspace, coupled with the spatial pattern of cell shapes, leads to the classically described palisade and spongy mesophyll histology of the typical angiosperm leaf. As a result of extensive investigations, we now have detailed knowledge of the plant cell cycle and, as a consequence, access to a number of

genes whose modulation leads to predictable changes in division rate and cell patterning and, as a consequence, leaf morphology (Dewitte et al., 2003; Verkest et al., 2005; De Veylder et al., 2007). In contrast, our understanding of the cell wall processes which lead to the controlled partial separation of cells subsequent to division (schizogeny) is much less advanced. Numerous enzyme activities (and associated genes) have the potential to modulate cell wall dissolution (McCann and Carpita, 2008), but how these activities are spatially and temporally co-ordinated with cell division within the leaf remains unclear. Thus although one might expect the patterning of intercellular airspaces to be altered as a consequence of altered cell size and packing, this downstream aspect of cell cycle gene manipulation has generally been overlooked, despite the fact that the core leaf physiological function of photosynthesis is likely to be significantly influenced (Flexas et al., 2008, 2008; Terashima et al., 2011). For example, altering cell size and packing is likely to alter the cell surface area available for gas diffusion, and the extent and tortuosity of the air channels linking photosynthetic cells to the stomata (which regulate entry and exit of $CO_2$ and water) will influence the diffusion of gases within the leaf. Although such structure/function relationships have long been recognised, they have generally involved correlating differences in leaf structure among different or related species rather than using molecular genetic techniques to manipulate structure within a species to identify causal relationships (Giuliani et al., 2013). We are interested in exploring the relationship between cell pattern and assimilatory physiology in the context of leaf development. Are there general rules relating cell division, growth and separation to the higher order architecture of the leaf, how do these rules relate to assimilatory physiology, and is there room for altering cell patterns to improve the efficiency of photosynthesis, a major target for crop improvement (Zhu et al., 2010)?

One reason for the lack of progress in this area has been the need for an easily implemented and robust methodology to detect and quantify leaf airspace in 3D. Classical approaches generally involve fixing tissue, taking sections, manually measuring airspace in these 2D sections, and then estimating the amount of 3D airspace (John et al., 2013). These approaches are labour intensive, invasive, and involve a number of assumptions about cell shape for the estimation of the values obtained. The advent of X-ray micro Computed Tomography (microCT) and its implementation to plant sciences has provided a new method to both visualize and quantify airspace in a non-invasive fashion (Cloetens et al., 2006; Dhondt et al., 2010). Living leaves can be scanned to generate 3D renderings of the internal architecture of the sample, easily distinguishing cellular material from the less dense airspace. These datasets can then be interrogated to derive various quantitative measures of airspace morphology such as porosity, exposed surface area, channel size and,

simultaneously, the arrangement of the tissues defining the airspace (Dorca-Fornell et al., 2013; Pajor et al., 2013). Moreover, the analysis can be delimited to specific regions of interest within the organ, thus enabling the exploration of potential linkages of local structure to whole organ function.

Variability in leaf airspace is not directly under genetic control, rather, it is an emergent property related to cell division, size and separation, and the consequences these have on cell packing. At present, the best tools we have to influence this packing (and thus intervening airspace) are various components of the plant cell cycle (De Veylder et al., 2007). Manipulation of these genes leads to changes in both cell size and cell packing. For example, numerous publications have shown that overexpression of *KIP-RELATED PROTEIN1 (KRP1)* tends to decrease proliferation, leading to larger cells (Dewitte et al., 2003; Verkest et al., 2005; Weinl et al., 2005; Kuwabara et al., 2011). Conversely, suppression of *RETINOBLASTOMA RELATED PROTEIN (RBR1)* can be used to generate organs with smaller cells (Wildwater et al., 2005) and, indeed, in a previous paper we reported on the establishment of a combined microCT/chlorophyll fluorescence and gas exchange analytical approach for Arabidopsis using an inducible RBR RNAi transgenic line as a test case (Dorca-Fornell et al., 2013). However, the uniform expression of the construct in this transgene led to changes in epidermal characteristics (notably stomatal density and associated stomatal conductance) which confounded clear interpretation of the outcome on mesophyll differentiation and function.

In this paper we set out to generate Arabidopsis leaves in which mesophyll cell proliferation was either promoted or repressed (using both *KRP1* and *RBR1* constructs) in order to investigate the outcome of resultant increased and decreased cell size on airspace pattern, and the consequence of such altered cell/airspace pattern on photosynthetic performance. Our data show that the generation of more, smaller cells in the mesophyll can lead to an increase in leaf photosynthetic capacity and implicate airspace pattern as an important factor in this process.

## RESULTS

### Modulation of cell cycle gene expression leads to altered leaf cellular architecture

To investigate the consequences of cell division inhibition on leaf mesophyll architecture we created transgenic plants in which the *KRP1* gene was expressed under control of an *RBCS* promoter sequence ($RBCS_{pro}$:KRP1) (see *Materials and Methods*). Our analysis focussed on leaf 8 at maturity. As expected, there was an increase in mean mesophyll cell size and a decrease in cell density compared to *Col-0* (WT) leaves (**Fig. 1A,B**). To quantify the

outcome on the amount and pattern of airspace, samples were subjected to microCT analysis. A 3D rendering of a portion of a WT leaf is shown in **Fig. 2A**, with paradermal sections through regions equivalent to the palisade and spongy layers shown in **Fig. 2E,I**. These can be compared with equivalent images of $RBCS_{pro}$:KRP1 leaves in **Fig 2B,F,J** which suggest an increased cell size and altered airspace distribution in the transgenic plants. The data sets were analysed to compare quantitative values for porosity, air channel diameter, circularity and density at different planes within the sample from the adaxial to the abaxial surfaces (**Fig. 2M-P**). These data showed that mean porosity (relative amount of airspace to total tissue volume) of *Col-0* WT tissue was generally low (15-20%) in the upper, adaxial part of the leaf (equivalent to the palisade region) but rose to a peak (30-35%) in the lower part of the leaf, the spongy tissue (**Fig. 2M**). When mean air channel diameter was measured, a similar distribution to porosity was observed (**Fig. 2N**), indicating that channels in the spongy region tended to be larger than those in the palisade layer. When channel circularity was considered, there was a minimum value towards the central part of the leaf (**Fig. 2O**), while air channel density in WT leaves declined in value across the palisade layer from the adaxial surface, reaching a minimum in the spongy region before rising towards the abaxial surface (**Fig. 2P**).

The $RBCS_{pro}$:KRP1 samples displayed a very similar pattern in all four parameters to WT but with the absolute values shifted. Thus, channel density was lower than WT in virtually all regions of the leaf (**Fig. 2P**) but channel diameter was similar to WT, with a slight shift in peak position reflecting the generally thicker mesophyll in these leaves (**Fig. 2N, Fig. S1B**). There was a shift to lower mean circularity values in the $RBCS_{pro}$:KRP1 samples (**Fig. 2O**), indicating a more varied shape of the air channels in most portions of the leaf. Despite these shifts in channel density and shape, the overall level and distribution of porosity in the $RBCS_{pro}$:KRP1 leaves was only slightly lower than WT (**Fig. 1C, Fig. 2M**).

In addition to targetting *KRP1* expression to the mesophyll, we also expressed the gene behind the *ATML1* promoter, leading to overexpression in the epidermis (see *Materials and Methods*) and, as expected, an increase in epidermal cell size (**Fig. S1A**). This manipulation also led to a significant decrease in mesophyll cell size and an increase in mesophyll cell density (**Fig. 1A,B**), substantiating previous observations (Bemis and Torii, 2007) and providing a set of transgenic plants displaying an inverse pattern of mesophyll cell size and density change to that observed in the $RBCS_{pro}$:KRP1 leaves. MicroCT imaging of the $ATLM1_{pro}$:KRP1 leaves suggested a higher tissue density in both the palisade and spongy layers (**Fig. 2C,G,K**) and quantitative analysis substantiated this impression. A much lower porosity level was measured throughout the leaf, as well as a generally smaller channel diameter (**Fig. 2M,N**). Channel circularity was higher than WT in the palisade region but

lower in the spongy, leading to an almost inverted pattern of channel circularity (**Fig. 2O**). When channel density was measured the pattern observed in the $ATLM1_{pro}$:KRP1 leaves was also distinct from that in WT and $RBCS_{pro}$:KRP1 samples, with a distinct peak occurring in the palisade region of the $ATLM1_{pro}$:KRP1 samples that was not observed in the other transgenic lines or WT plants (**Fig. 2P**).

We also targetted increased mesophyll cell division by expressing an RBR1 RNAi construct using the *CA1* promoter sequence (see *Materials and Methods*). Suppression of RBR1 is expected to relieve the brake on cell division, leading to the accumulation of more but smaller cells in the mesophyll (Kuwabara et al., 2011). Analysis of the $CA1_{pro}$:RBRi leaves indicated that mesophyll cell size was decreased relative to WT, with a concomitant increase in cell density, although these changes were not as great as observed in the $ATLM1_{pro}$:KRP1 leaves (**Fig. 1A,B**). MicroCT analysis of the $CA1_{pro}$:RBRi samples (**Fig. 2D,H,L**) indicated a general decrease in porosity in the adaxial and spongy regions and a decrease in mean channel diameter, coupled with slight shifts in channel circularity and density compared with WT samples, but with the overall patterns of these parameters being similar to those observed in WT leaves (**Fig. 2M-P**)

**Increased mesophyll cell density leads to an increase in photosynthetic capacity**

To investigate whether the altered patterns of cellular architecture described above were linked to any change in physiological performance, we performed a combined fluorescence/gas exchange analysis on the same leaf samples used for microCT. These data revealed a tendency for higher $A_{sat}$ (maximum assimilation rate under saturating $CO_2$) in all three transgenic lines relative to WT, with significant increases ($P<0.05$) in the $CA1_{pro}$:RBRi and $ATLM1_{pro}$:KRP1 lines (**Fig. 3A**). The pattern of decrease in porosity in the palisade layers (**Fig. 3C**) generally mirrored the pattern of $A_{sat}$ increase, suggesting that there might be a causal link, with the link to porosity of the spongy layers (**Fig. 3E**) being less obvious. To investigate the potential underpinning mechanism for these observations we performed a number of further analyses.

Firstly, $A_{sat}$ is measured on a per area basis, thus an increase in $A_{sat}$ might reflect an increase in photosynthetic capacity per solid tissue volume or an increase in leaf thickness (with no change in photosynthetic capacity per tissue volume), or a combination of these changes. When the data shown in **Fig 3A** were normalised for porosity, a similar pattern of assimilation rates was still observed (**Fig. 3B**), suggesting that the increased tissue density resulting from altered cell division pattern did not account for all of the observed increases in $A_{sat}$. In contrast, normalisation for differing leaf thickness led to assimilation rates in the $RBS_{pro}$:KRP1 and $CA1_{pro}$:RBRi lines similar to those calculated for WT samples (**Fig 3D**).

However, when the different lines were compared for assimilation rate after normalisation for both leaf thickness and mesophyll porosity, the ATML1$_{pro}$:KRP1 samples still showed a significantly higher rate of $CO_2$ assimilation, whereas the other two lines could not be distinguished from WT (**Fig 3F**).

One possibility for the higher assimilation rate per solid leaf volume in the ATML1$_{pro}$:KRP1 line was that there had been an upregulation of photosynthetic capacity. To investigate this possibility we first assayed the ability of the tissue to absorb and utilise light by directly measuring light absorptance (**Fig S2A**), assessing the fraction of light energy directed to photosystem II, αβ (**Fig. S2C**), the maximum efficiency of photosystem II, $F_v/F_m$ (**Fig. S2E**) and the initial/maximum quantum yield for $CO_2$ fixation, $Y(CO_2)_{LL}$ (**Fig. S2G**). These assays indicated no difference between any of the lines. Measurement of total pigment levels in the leaves did indicate a significantly higher concentration in the ATML1$_{pro}$:KRP1 leaves (**Fig. S2F**) but measurement of total leaf protein did not indicate any major increase in the ATML1$_{pro}$:KRP1 samples, suggesting that the total amount of Rubisco was not altered in a major way (**Fig. S2H**). However, calculation of $V_{cmax,}$ which is a measure of the maximal Rubisco activity *in vivo* (von Caemmerer and Farquhar, 1981) indicated that the ATML1$_{pro}$:KRP1 tissue had a significantly increased $V_{cmax}$ (**Fig. 4A, Fig. S4C**), consistent with the measured increase in $A_{sat}$ and *CE* (**Fig. S2B**). Overall, this evidence suggests that the measured increase in *A* was not a reflection of an increased maximum efficiency of the photochemical machinery or amount of Rubisco, but rather in an increase in the proportion of light energy utilisation through a reduced quenching of PSII in operational conditions, increased operational electron transport rate, *J* (**Fig. S2D**) and an increased Rubisco activation state.

**Analysis of mesophyll conductance and airspace pattern**

The rate of carbon fixation can also be influenced by the supply of $CO_2$ and we therefore performed a series of analyses to test this hypothesis. Consistent with this proposal, there was a higher mesophyll conductance ($g_m$) in the ATML1$_{pro}$:KRP1 leaves than in WT (**Fig 4C**), indicating a lower resistance to $CO_2$ flux from the leaf airspaces to the active sites of Rubisco $CO_2$ fixation within the chloroplasts. This leads to an ameliorated ratio between Rubisco carboxylation and photorespiration, allowing higher net assimilation for a given level of electron transport. The exposed mesophyll surface area ($S_m$) is expected to play an important role in determining $g_m$ since gas diffusion into and out of cells in the leaf must occur via the cell surfaces (Terashima et al., 2011) and is significantly slower in water than in air. However, analysis of $S_m$ did not reveal any significant difference between the different lines except in the CA1$_{pro}$:RBRi samples, which displayed a lower value of $S_m$ (**Fig 4B**). Mesophyll conductance can also be influenced by physical parameters such as cell wall

thickness and the arrangement and/or proximity of the chloroplasts to the plasma membrane of mesophyll cells. However, analysis of these parameters did not reveal any overt change which might account for the higher $g_m$ in the $ATML1_{pro}$:KRP1 leaves (**Fig S3**). For example, mesophyll walls in the $ATML1_{pro}$:KRP1 cells had an average thickness of 0.164 µm +/- 0.03 µm whereas WT mesophyll cells had a average thickness of 0.096 µm +/- 0.008 µm. Thus the $ATML1_{pro}$:KRP1 mesophyll cell walls were actually thicker than WT (t-test. $P < 0.05$, $n > 4$), which might, if anything, be expected to decrease $CO_2$ conductance.

The air channel network in a leaf is involved both in the influx of $CO_2$ and the efflux of water vapour, so that altered evapotranspiration might also influence the measured rate of $CO_2$ assimilation (Terashima et al., 2011). Although the $CA1_{pro}$:RBRi leaves had a higher stomatal density (**Fig. S1B**) there were no significant differences between the other lines investigated and the measured stomatal conductance was not significantly different between any of the lines (**Fig. S1C**), arguing against this having a major effect on $A_{sat}$ or $V_{cmax}$. An analysis of the relative roles of stomatal and non-stomatal limitations on assimilation indicated that stomatal limitation increased in the $ATML1_{pro}$:KRP1 leaves (**Fig S4A,B**), co-inciding with the increase in $V_{cmax}$ (normalised for both leaf thickness and porosity) (**Fig. S4C**). Overall, this evidence is consistent with the idea that greater *in vivo* Rubisco activity shifts the control of photosynthesis away from photosynthetic capacity and towards $CO_2$ entry into the leaves.

Since our microCT analysis had revealed that the $ATML1_{pro}$:KRP1 leaves showed a distinct change in the pattern of air channel density and the most extreme decrease in channel diameter (**Fig. 2 N,P**), we took a closer look at these structural parameters across all four of the lines used. Consideration of palisade channel diameter (**Fig. 4D**) and mean palisade channel density (**Fig. 4E**) suggested some degree of correlation of these structural parameters with the measured physiological parameters of $A_{sat}$ and $V_{cmax}$. A correlation analysis of the various structural parameters and leaf performance measures reported in this paper indicated a number of potential relationships, however most of these were not significant at the 0.05 confidence level. The exceptions to this were an inverse relationship of $A_{sat}$ and spongy mesophyll porosity ($r^2 = 0.82$, $p = 0.03$) and $A_{sat}$ and mean air channel diameter ($r^2 = 0.78$, $p= 0.047$). Most striking was the correlation between palisade air channel diameter and $V_{cmax}$ ($r^2 = 0.97$, $p = 0.019$), supporting a tight linkage of these traits.

A deeper analysis of the air channel networks revealed further structural differences between the leaves that might influence photosynthetic performance. Representative images of the skeletonised palisade and mesophyll layers from control and $ATML1_{pro}$:KRP1 leaves are shown in **Fig. 5A-D**. The networks are colour coded so that green indicates regions where there are more than 2 connections per voxel and magenta indicates regions where

there are fewer than 2 connections per voxel (equivalent to end points in the network). The palisade layer of the ATML1$_{pro}$:KRP1 leaves was characterised by having fewer visible regions of high connectivity and an apparently higher density of network endpoints (magenta colour) (compare **Fig 5A,B**). Quantitative analysis of the air space networks (**Fig. 5E-H**) showed that the palisade layer of the ATML1$_{pro}$:KRP1 leaves was characterised by a decrease in mean branch length and a network in which there were markedly fewer branch connections per leaf volume, i.e., network connectivity was significantly decreased (**Fig. 5G**). As a consequence, the ATML1$_{pro}$:KRP1 palisade layer air channel network displayed a significantly lower tortuosity (a measure of the twistedness of branches per volume) than WT palisade tissue (**Fig. 5H**).

## Discussion

### The impact of altered cell division patterns on leaf airspace amount and distribution

In this investigation we used targeted expression of cell cycle genes expression to alter cell division patterns in the leaf mesophyll with the aim of investigating the outcome on airspace patterning. As expected, expression of *KRP1* in the mesophyll led to the formation of fewer but larger cells whereas directing *KRP1* expression to the epidermis led both to an increase in epidermal cell size and a decrease in mesophyll cell size (Verkest et al., 2005; Weinl et al., 2005; Kuwabara et al., 2011). Previous publications have shown that *KRP1* fusion proteins have the ability to move between cells and that the outcome of *KRP1* on the cell cycle may be both level and context dependent, leading to the proposal that low levels of KRP1 may act to license entry to G1 phase of the cell cycle (Verkest et al., 2005). Although the precise mechanism by which epidermal-directed expression of KRP1 leads to an effect on sub-epidermal cell size remains to be elucidated (Bemis and Torii, 2007), our data show that it can be reliably used as a tool to modify mesophyll cell division. Similarly, the observed decrease in palisade cell size and increase in cell density in the *CA1$_{pro}$:RBRi* transgenic leaves is consistent with the established role of this protein in suppressing cell proliferation (Borghi et al., 2010; Gutzat et al., 2012). Thus, by targeting expression of well-characterised cell cycle genes to different parts of the leaf we were able to generate plants with a spectrum of mesophyll cell size and density and, consequently, cell packing.

Our data clearly indicate that altering cell division pattern has a knock-on effect on the pattern and extent of air-space formation in the leaf, as well as cell size. The mechanism by which this happens is essentially unknown. An array of cell wall enzymes are required for the controlled breakdown of cell wall components to allow for cell separation (McCann and Carpita, 2008). The simple observation that, for example, eudicot leaves generally form

distinct palisade and spongy layers indicates that there is a strong genetically programmed control of these processes. At the same time, it is clear that environmental influences modulate the extent of these cell separation processes and one can envisage complicated feedback systems whereby altered cell division patterns lead to different physiological constraints within a tissue which might feed into cell size and separation to ensure an appropriate balance of, e.g., surface area for gas/vapour diffusion and photosynthesis/transpiration. Unravelling the molecular mechanism by which these cell wall changes are affected and integrated at a local and organ level with cell growth and division remains a major challenge for future research.

Use of microCT allowed us to quantify the outcome of these altered cell division patterns on 3D airspace patterning. The results showed that modulation of leaf cell size and density does lead to modulation of intervening airspace, but that the outcome is dependent on the manipulation performed. Thus, promotion of smaller cells in the mesophyll was associated with an increase in channel density and a decrease in channel diameter, with a concomitant decrease in overall leaf porosity, i.e., a denser mesophyll was generated. Although repression of mesophyll cell division led to an increase in cell size and a decrease in channel density, the concomitant changes in channel diameter and shape meant that the overall change in leaf porosity was very limited. The different outcomes on air channel amount and patterning of the different manipulations suggests that these are not simple scaling outcomes related to altered cell size, rather that there are feedback mechanisms relating cell size/shape and airspace within a leaf. The molecular mechanisms for these feedback processes remain obscure but add to a picture (demonstrated, for example, by the phenomenon of compensation in leaves) in which size is somehow measured at a global scale so that the local scale is adjusted accordingly to produce a functional organ (Hisanaga et al., 2015). Whether physiological or biochemical activities act as part of the spatial mechanism of growth/function integration is open to speculation.

The use of 3D imaging allowed us to quantify the distribution of airspace across the leaf adaxial/abaxial axis. As expected, WT leaves displayed the classically described pattern in which relatively small channels at high density characterised the adaxial palisade region, whereas the abaxial spongy region contained relatively large channels at lower density. In the transgenics in which cell division was manipulated this pattern was generally shifted up or down relative to WT, suggesting that altered cell proliferation was modulating the developmental pattern rather than obliterating or radically changing it. This fits with our understanding of the adaxial and abaxial leaf domains being set early in development via a complex hierarchy of transcription factors and signalling events (Braybrook and Kuhlemeier, 2010). Although cell cycle genes must be part of the downstream effector network by which

these patterns are translated into palisade and spongy differentiation, altered cell division alone does not generally appear sufficient to mask this initial pattern. However there was an exception to this rule. In the ATML1$_{pro}$:KRP1 plants (which showed the greatest decrease in cell size and increase in cell density) there was an abnormal and marked peak of channel density in the palisade. As far as we are aware, such a shift in airspace pattern has not been previously reported. These results show, firstly, that air channel pattern can be significantly manipulated within a leaf via modulation of cell division pattern. Secondly, as discussed below, such shifts in airspace channel pattern and size may underpin significant changes in photosynthetic performance.

**Altered cell division pattern, airspace and photosynthetic performance**

Both an increase in mesophyll cell size and a decrease in mesophyll cell size tended to increase leaf photosynthetic rate (**Fig. 3A**). However, the mechanisms underpinning these measured increases were distinct. With respect to increased cell size, although there was a slight decrease in spongy porosity (indicating some increase in tissue density), the majority of the increase in photosynthetic rate measured per leaf area could be accounted for by an increase in leaf thickness. The simplest interpretation is that the increase in mesophyll cell size led to an increase in the depth of photosynthetic tissue in which gas exchange was measured, with little outcome of altered cell packing on photosynthetic performance. With respect to the leaves in which mesophyll cell size was decreased, the situation was more complicated. Neither increased leaf thickness nor the increased tissue density resulting from these manipulations accounted for all of the measured increase in photosynthetic rate in the leaves with the most extreme cellular phenotype. Assays of photosynthetic biochemistry did not suggest any major shift in either the ability of the tissue to absorb light energy or capacity to transfer this energy into carbon fixation. However, there was evidence of a significant change in the in vivo activity of the carbon fixing enzyme Rubisco that underpinned the observed improvement in photosynthetic performance in this line. An additional possibility is that the structural changes resulting from the generation of a mesophyll containing such small cells somehow led to an increased $CO_2$ conductance within the leaf.

Mesophyll conductance ($g_m$) is a complex trait which has been postulated to play an important role in photosynthetic efficiency (Flexas et al., 2008; Kaldenhoff, 2012; Adachi et al., 2013). Essentially, an improved flux of $CO_2$ within the mesophyll should lead to a better supply of $CO_2$ to Rubisco, hence an improved rate of carbon fixation. In support of this hypothesis, $g_m$ was higher in the ATML1$_{pro}$:KRP1 line compared to both WT and the other transgenic lines. Measurements of structural parameters that might influence $g_m$ (exposed mesophyll surface area, chloroplast distribution within the mesophyll cells, mesophyll cell wall thickness) did not reveal any changes in the ATML1$_{pro}$:KRP1 samples which might

underpin the observed increase in $g_m$. In contrast, distinct structural changes were observed in this line which can plausibly be traced to the manipulation performed. These included a high palisade air channel density, a significant decrease in air channel diameter, and a decrease in air channel connectivity and tortuosity. Predicting the outcome of such altered air channel pattern and dimensions on diffusion within a leaf and gas exchange with surrounding tissue is not trivial and requires various assumptions on, e.g., laminar gas flow, distribution of $CO_2$ sinks within the leaf, as well as estimations of the counter flow of water vapour within the same channels (Parkhurst, 1994). Nevertheless, the altered structural parameters of the airspace network in the palisade of the $ATML1_{pro}$:KRP1 leaves are consistent with a network in which $CO_2$ is expected to permeate more rapidly and to a higher resolution, thus potentially decreasing the pathway length for $CO_2$ diffusion in the liquid phase. Such changes would contribute to the observed increase in $g_m$ and increased maximum assimilation rate. A greater understanding and modelling of the local concentrations and flux of $CO_2$ and water vapour within the mesophyll air channel networks will be required to test this hypothesis.

In conclusion, the results reported here indicate that altered cell division patterns in the leaf lead to altered patterns of airspace and can lead to an increase in photosynthetic rate. Although some of this increase can be related to changes in gross leaf morphology (thicker leaves) and internal cellular architecture (less porous, denser leaves containing smaller cells), leaves with more extreme increases in cell density appear to have other factors at play, namely increased Rubisco activity and higher $g_m$. We propose that the generation of a higher density network of shorter, smaller diameter but less connected air channels in the palisade layer plays a role in the measured increase in $g_m$. Our data indicate that a complex interaction of cell division patterning, growth and separation informs airspace patterning, with the integration of these factors having a major influence on leaf photosynthetic performance. The molecular mechanisms co-ordinating these cellular and organ-level processes await elucidation.

## MATERIALS AND METHODS

### Plant Growth

Seeds were stratified on wetted filter paper at 4°C in the dark for 7 days, then germinated on M3 compost in 4 x 4 x 6 cm brown plastic pots. All plants were grown in a Conviron MTPS 120 growth room (Manitoba, Canada) with a 12 hour photoperiod set to 21/15°C day/night temperatures, 60% relative humidity (RH), and 200 µmol $m^{-2}$ $s^{-1}$ photosynthetic photon flux density (PPFD) at canopy height. Only leaf 8 of replicate plants was subjected to absorption measurements, pigment content quantification, or combined fluorescence/gas exchange and

subsequent microCT analysis, as described below. For all measurements, leaf 8 was sampled between 34 and 38 days after sowing, a time by which leaf 8 had reached its final size but had not undergone any obvious signs of senescence. For Dex induction, 10 µl of 10 µM Dex/DMSO solution was applied to the shoot apex on days 15, 16, and 17 when leaf 8 was initiated. Forty-eight hours after the final Dex application, a leaf from at least three representative plants each was harvested for GUS assay.

For selection of transgenic lines, seeds were surface sterilized, stratified at 4°C in the dark for 7 days, then grown for selection on half-strength Murashige and Skoog salt mix (Sigma-Aldrich, USA), 1% (w/v) sucrose and 0.8% (w/v) plant agar (Duchefa Biochemie, The Netherlands) with appropriate antibiotic selection (20 µg $ml^{-1}$ hygromycin or 50 µg $ml^{-1}$ kanamycin). Plates were kept in a growth chamber (Snijders Scientific, The Netherlands) with a 16 hour photoperiod at 100 µmol $m^{-2}$ $s^{-1}$ PPFD and constant temperature 22°C before either collection for analysis or transfer to M3 soil for seed production in a 16 hour photoperiod, at 22°C constant temperature, 60% RH, and 100 µmol $m^{-2}$ $s^{-1}$ PPFD at canopy height.

**Creation of transgenics and mutant characterisation**

The transgenic line *$RBCS_{pro}$:KRP1* was made by introducing a previously described GUS.YFP.KRP1 sequence in the Gateway compatible pEN01 vector (Weinl et al., 2005) by gateway recombination into pRBC-pAM-PAT-GW where the 35S promoter has been exchanged with the subepidermal specific promoter $RBCS2b_{pro}$ (Kim et al., 2005) using restriction site cloning. Targeting of KRP1 under control of the *RBCS2b* promoter was expected to lead to expression of the gene predominantly in the mesophyll. Localization of transgene expression to the mesophyll was confirmed via GUS histochemical analysis (**Fig S5E**), although some staining was also observed in the epidermis. For this line (and others described below) measurements of cell size and density were obtained across 12 images, each with approximately 15 cells, from at least three independent plants using ImageJ software.

The transgenic line *$ATML1_{pro}$:KRP1* was constructed by introducing a previously described YFP.KRP1 sequence (Weinl et al., 2005) behind the $ATML1_{pro}$ via Gateway recombination cloning. The construct was introduced using gateway recombination into the vector pATML1-pAM-PAT-GW that has been previously described (Bouyer et al., 2008) and transformed into *Arabidopsis thaliana* (*Col-0*) using a conventional floral dip method. Seeds were collected and, after selection based on the antibiotic selection marker, used to generate homozygous T3 lines (confirmed by genotyping) which were used for experiments. Epidermal expression

was confirmed by confocal microscopy using the YFP tag included in this construct (**Fig S5H**). This revealed relatively large epidermal cells, confirmed by measurements (**Fig. S1A**).

The line $CA1_{pro}$:RBRi was made by first introducing a 2124bp fragment of the PPCA1 promoter from *Flaveria Trinervia* (Gowik et al., 2004) into a Dex inducible/ LhGR activator construct pBin-LR-LhGR$^2$, which also contains the GUS reporter gene sequence (a gift from I.Moore) by gateway cloning. The promoter was amplified using primers: 5' CACCAAGGACTCACCAGGACAGG 3' and 5' TACTCACACCCTTGCTTAATAC 3', using pPPCA1-pAM-PAT GW as template (Bouyer et al., 2008). In order to clone the RBRi sequence we used CATMA3a11240 GST (N264209, NASC stock centre) (which contains a 169 bp fragment of the RBR1 gene (AT3G12280)) to clone into pOpOff1 (RNAi construct, gift from I.Moore) by Gateway cloning. Both constructs, pBin-LR-LhGR$^2$:pPPCA1 and pOpOff1:RRBi, were transformed independently into *Col-0* using a conventional floral dip method. Homozygous T3 lines were obtained for each construct and crossed together in order to obtain lines that expresses RBRi under the dex-inducible CA1 promoter. Homozygous $CA1_{pro}$:RBRi lines were used for further analysis, with GUS histochemical analysis of induced tissue revealing target gene expression was restricted to the mesophyll (**Fig S5K**). Although $CA1_{pro}$:RBRi lines showed a decrease in palisade cell size (**Fig. 1A**), this was observed in both induced and non-induced lines and qPCR analysis did not indicate a significant reduction in transcript level after induction (two independent transgenic lines). In the experiments described for the analysis of leaf cellular architecture and physiology, data for induced and non-induced lines were combined since they did not separate in subsequent analyses but were distinct from *Col-0*.

**GUS histochemistry**

For analysis of GUS reporter gene expression plants were submersed in X-GlcA substrate (5 bromo-4-chloro-3-indolyl ß-D-glucuronic acid cyclohexylammonium salt, 0.5mg/ml) in 100 mM $NaH_2PO_4$ (pH 7.0) in the presence of potassium hexacyanoferrate II +III (1mM) at 37°C overnight, after vacuum infiltration for 20min. Samples were rinsed in 70% v/v ethanol and fixed in 100% EtOH:glacial acetic acid (7:1 v/v) at RT overnight until complete removal of chlorophyll. Samples were embedded for sectioning using Technovit 7100 (Heraeus Kulzer) following the manufacturer's instructions. Sections (8µm) were taken using a Leica RM 2145 microtome. After staining with 0.02%(w/v) Saffranin O samples were observed under an Olympus BX51 light microscope.

**Gas exchange and fluorescence measurements**

Fluorescence and gas exchange were simultaneously measured with a LI-6400 XT equipped with a 2cm$^2$ leaf chamber fluorometer (Li-6400-40; LI-COR, USA). For all

measurements, leaf temperature was maintained at 21°C and cuvette RH was controlled at c. 60% to match growth conditions. In order to minimise diffusive limitations, light response curves were performed at a $CO_2$ concentration in the measurement cuvette ($C_a$) of 1000 µL $L^{-1}$, under decreasing irradiance, from 1500 to 0 µmol $m^{-2}$ $s^{-1}$ *PPFD*. $F_v/F_M$ was measured on dark-adapted leaves at 400 µL $L^{-1}$ $C_a$. $A/C_i$-response curves were measured on six replicate plants per genotype at 1200 µmol $m^{-2}$ $s^{-1}$ PPFD. Leaves were pre-acclimated for about 20 minutes at $C_a$=100 µL $L^{-1}$ to induce stomatal opening, once $g_s$ had reached a threshold of 0.3 mol $H_2O$ $m^{-2}$ $s^{-1}$, $C_a$ was set to 400 µL $L^{-1}$ $CO_2$, and acclimated until $A$ and $g_S$ were stable. $A/C_i$ curves were measured at $C_a$ values of 50, 100, 150, 200, 250, 300, 400, 500, 600, 800, 1000, 1300 and 1600 µL $L^{-1}$, following (Long and Bernacchi, 2003; Evans, 2014). For each leaf measured, an $A/C_i$ curve was first performed at ambient oxygen concentrations (*i.e.,* approximately 21%), and then a second $A/C_i$ curve with identical settings was performed with the cuvette atmosphere supplied with 2% $O_2$. Steady-state values of $g_s$ were taken or calculated at $C_a$ of 400 µL $L^{-1}$ during the $A/C_i$ curve measurements at ambient $O_2$ concentration.

Light- and $A/C_i$-response curves were analysed following (Bellasio et al., 2016). Briefly, the PPFD dependence of gross assimilation (*GA*) was described empirically by a non-rectangular hyperbola so as to estimate, by iterative fitting, the respiration in the light ($R_{LIGHT}$), the maximum quantum yield for $CO_2$ fixation ($Y(CO_2)_{LL}$) as the initial slope of the light-response curve [$Y(CO_2)_{LL}$] and the light-saturated *GA* ($GA_{SAT}$) as the horizontal asymptote. The light compensation point (*LCP*) was estimated by solving the fitted light-response curve for $GA = R_{LIGHT}$. An empirical non-rectangular hyperbola was fitted to the $A/C_i$ curves under ambient and low $O_2$ to estimate the maximal carboxylating efficiency (*CE*) as the initial slope, the $C_i/A$ and $C_i/GA$ compensation points (Γ and $C_i^*$, respectively) and the $CO_2$-saturated $A$ ($A_{SAT}$). The *in vivo* Rubisco specificity factor ($S_{C/O}$) was estimated under the assumption that Γ* and $C_i^*$, from all-plants-averaged $C_i^*$ (47.3 µmol $mol^{-1}$) (Brooks and Farquhar, 1985) and resulted in an $S_{C/O}$ estimate of 2114 bar $bar^{-1}$. Thus, these values were used in the curve fitting procedure for all genotypes. The fraction of *PPFD* harvested by PSII (a quantity called αβ) was derived by linear regression of *Y(II)* plotted against the quantum yield for $CO_2$ fixation ($\Phi_{CO2}$, or $Y(CO_2)$ here) using data from the $A/C_i$ curve measured under low $O_2$ (Valentini R., 1995). With αβ, $b$, and measured values of *Y(II),* the electron transport rate (*J)* was derived for each point of the $A/C_i$ curve measured under ambient $O_2$ (Valentini R., 1995). Mesophyll conductance to $CO_2$ diffusion ($g_m$) was estimated using the NRH-A variant of the method proposed by Yin and Struik (Yin and Struik, 2009) using the lesser root to the equation A23 from von Caemmerer (von Caemmerer, 2013) by iterative fitting $A$ from the $A/C_i$ curves, with $J$ and $R_{LIGHT}$ previously derived. The $CO_2$ concentration at the site of

Rubisco carboxylation ($C_C$-based Rubisco kinetic parameter $V_{CMAX}$) was estimated by fitting the 'full Farquhar model' as developed by Ethier and Livingston (Ethier, 2004) to the Rubisco-limited part of the $A/C_i$ curve, with Γ, $g_M$, and $R_{LIGHT}$ previously determined and $K_C(1+O/K_O)$ assumed (560 µbar).

$A_{sat}$ values were normalised for mesophyll thickness and/or porosity using paired data obtained from CT scans of the same leaves used for gas exchange analysis (described below). These data are provided in Supplementary Table 1.

**Absorptance and pigment analysis**

Light absorptance was measured in the same central region of the leaf where both photosynthesis and microCT measurements were taken (Rackham, 1968). Leaves were irradiated using two lasers: a blue diode-pumped solid-state laser (Laser 2000, UK, emission 468 and 472 nm), and a red supercontinuum laser (Fianium Ltd., UK, emission 495 and 700 nm). Radiation was measured with a Taylor-type integrating sphere (Labsphere Inc., USA), and a spectrometer with a 50 µm slit, a diffraction grating blazed at 500 nm and a spectral range between 300 and 720 nm (Oriel, USA). Total light absorptance of a leaf was then calculated as the average absorptance of all wavelengths measured across 468 and 472 nm and 495 and 700 nm. Photosynthetic pigments were quantified on four replicate plants per genotype. Two discs (8.5 mm diameter) were punched from each side of the midrib, fresh weight measured, and rapidly ground with 80% (v/v) acetone. Visible spectra was measured (400 and 700 nm) at 1 nm steps and total pigment levels quantified according to (Lichtenthaler and Wellburn, 1983).

**X-ray Micro Computed Tomography (CT) image acquisition and analysis**

Leaf 8 of each plant was imaged using an X-ray micro CT scanner (Nanotom, General Electric Company, USA) in two steps; whole leaf imaging to investigate leaf morphological features and imaging of two leaf discs (5 mm diameter). These discs were cut symmetrically from each side of the mid-rib. Samples were kept static during image acquisition to maximize image quality. CT scans of the whole leaves were obtained at spatial resolution of 15 µm with energy of 65 kV and 140 µA, collecting 720 projections with an exposure time of 750 ms resulting in the total scan time of 18 min per leaf. Datasets of leaf discs were acquired at 2.75 µm of spatial resolution, using the same energy and exposure settings as for the whole leaf but collecting 1200 projections resulting in total scan time of 30 min per leaf disk.

2D projections (radiographs) acquired during the scans were reconstructed (Datos|X; General Electric Company, USA) into 3D volumes using a filtered back-projection algorithm, rendered, and converted into stacks of Tiff images (VG Studio Max version 2.2; Volume Graphics, Germany). Image stacks were used to create a mask separating the leaf or leaf discs from the background and any holding devices (Avizo version 6.0; FEI, USA). In case of whole leaf datasets, the masks were directly quantified using the ImageJ plugin BoneJ (http://bonej.org/). Image stacks with leaf discs separated from the background were cropped to remove any damaged area on the edges. Cropped and aligned image stacks of leaf discs were thresholded using Image J IsoData and minimum algorithms to obtain stacks of images representing the leaf disc mask and plant material only. The generated image stacks were used as the input to the ImageJ image calculator and the function XOR was used to generate image stacks with only pore space visible. As the last stage of image analysis, the structural descriptors of intercellular pore space such as porosity, channel diameter, mesophyll surface area, connectivity, circularity and skeleton analysis were obtained using the ImageJ particle analyser and BoneJ. 3D renderings of connected channel networks were generated using RGB stacks from ImageJ imported into VG Studi Max. For analysis we defined a region of interest between the boundary of the upper epidermis/mesophyll and lower epidermis/mesophyll. This allowed us to use mesophyll thickness (rather than leaf thickness) in our analysis of photosynthetic parameters. Mesophyll surface area was normalized to the one-sided surface area of the leaf disc to calculate the 'exposed mesophyll surface area' parameter. Two subsets of the porosity, channel diameter, and circularity data were taken along the thickness of each leaf, at distances of one quarter and three quarters from the adaxial surface to represent palisade and spongy mesophyll types, respectively. For network analysis, tortuosity was calculated as branch length/Euclidean distance, where Euclidean distance is the mean distance (mm) between the V1 and V2 vertices (end points) of each branch within a volume.

**Confocal and standard light microscopy**

For light microscopy, leaves were dehydrated in an ethanol series, fixed in a 7:1 ethanol: glacial acetic acid solution, then imaged using differential interference contrast microscopy (Kuwabara et al., 2011Kuwabara et al., 2011) (**Fig S5A-D,F,G,I,J**)**.** Cleared leaves were photographed using imaging software (Cell B, Olympus, Hamburg, Germany) and a DP71 camera on an Olympus BX51 (Hamburg, Germany). Confocal images from living leaves were collected using an Olympus FV1000 with SIM-scanner on a BX61 upright microscope, with Olympus FluoView FV1000 software. Chlorophyll excitation was at 488nm and emission was between 650 and 710nm. YFP was excited at 515nm and emission collected between

530 and 570nm. Gain and offset levels were kept constant during all measurements. Three different plants were imaged per line and two leaf discs were collected per leaf from either side of the midrib then mounted in perfluorodecalin. Two areas were imaged in each leaf disc. A z-stack was taken of the palisade mesophyll layer with a stepsize of 1µm, and the clearest parts of the images of the chloroplasts were merged in Adobe Photoshop CS2 to give representative images for analysis.

**Transmission electron microscopy**

Samples were fixed in 3%(w/v) glutaraldehyde in 0.1M sodium cacodylate buffer overnight, washed twice in same buffer (15 min each) then post-stained 1%(w/v) osmium tetroxide for 1 hr. After a brief rinse in water, samples were washed twice for 15 min in cacodylate buffer, then dehydrated through an aqueous ethanol series (50%, 75%, 80%, 90%, 95%, 100%), 15 min each wash. After two 15 min washes in epoxypropane (EPP), samples were infiltrated in 50% (w/v) araldite resin in EPP overnight on a rotor. The solution was replaced with fresh araldite resin twice over 8 hrs on a rotor. Samples were then embedded in fresh araldite resin in coffin moulds and left at 60°C to cure for 2-3 days. Sections (85nm) were then taken using a Leica UC6 and collected onto 400 mesh Formvar copper grids. After staining in uranyl acetate and Reynold's lead citrate, sections were viewed on an FEI tecnai Biotwin TEM at 80kV. Images were recorded on an Orius digital camera using Gatan digital micrograph. Samples were taken from at the middle of the lamina on mature leaf 8 from at least 4 independent plants and multiple images taken from sections from each tissue block. For analysis of cell wall thickness, care was taken to ensure that sections were perpendicular to the wall, as indicated by sharp boundaries within the image and minimal indication of shearing.

**ACKNOWLEDGEMENTS**

We thank Chris Hill for his help in the analysis of the TEM samples and Ashley Cadby for access to the integrating sphere.

**Competing Interests:** The authors have no competing interests.

**Author Contributions:** CL, RP, MRL, AM, JS, MB, AM, AD, DB performed the experiments; CL, RP, MRL, AM, JS, CB, DB, AS, CS, CPO, SR, SM, AJF analysed the data; CL, RP, MRL, AM, DB, AS, CS, SM, AJF designed the experiments; CL, RP, MRP led on the organisation and management of different parts of the project; CL, RP, MRL, CB, AS, CS, CPO, SR, SM, AJF contributed to writing the manuscript; SM and AJF planned and led the project.

**Funding.** The project was funded by BBSRC grant BB/J004065/1 “Optimising photosynthetic efficiency via leaf structure”.



## SHORT SUPPORTING INFORMATION LEGENDS

**Sup Fig. S1.** Epidermal cell size, stomatal density and stomatal conductance.

**Sup Fig. S2.** Analysis of light absorption and photosystem efficiency.

**Sup Fig. S3.** Analysis of chloroplast and cell structure.

**Sup Fig. S4.** Analysis of stomatal and non-stomatal limitation.

**Sup Fig S5.** Generation and characterisation of transgenic Arabidopsis.

**Sup Table S1.**

## REFERENCES

**Adachi S., Nakae T., Uchida M., Soda K., Takai T., Oi T., Yamamoto T., Ookawa T., Miyake H., Yano M. and Hirasawa T.** (2013) The mesophyll anatomy enhancing CO2 diffusion is a key trait for improving rice photosynthesis. Journal of Experimental Botany **64:** 1061-1072

**Bellasio C., Beerling D.J. and Griffiths H.** (2016) An Excel tool for deriving key photosynthetic parameters from combined gas exchange and chlorophyll fluorescence: theory and practice. Plant Cell Environ **39:** 1180-1197

**Bemis S.M. and Torii K.U.** (2007) Autonomy of cell proliferation and developmental programs during *Arabidopsis* aboveground organ morphogenesis. Dev Biol **304:** 367-381

**Borghi L., Gutzat R., Futterer J., Laizet Y., Hennig L. and Gruissem W.** (2010) Arabidopsis RETINOBLASTOMA-RELATED is required for stem cell maintenance, cell differentiation, and lateral organ production. The Plant Cell **22:** 1792-1811

**Bouyer D., Geier F., Kragler F., Schnittger A., Pesch M., Wester K., Balkunde R., Timmer J., Fleck C. and Hulskamp M.** (2008) Two-dimensional patterning by a trapping/depletion mechanism: the role of TTG1 and GL3 in Arabidopsis trichome formation. PLoS biology **6:** e141

**Braybrook S.A. and Kuhlemeier C.** (2010) How a plant builds leaves. Plant Cell **22:** 1006-1018

**Brooks A. and Farquhar G.D.** (1985) Effect of temperature on the CO2/O 2 specificity of ribulose-1,5-bisphosphate carboxylase/oxygenase and the rate of respiration in the light : Estimates from gas-exchange measurements on spinach. Planta **165:** 397-406

**Cloetens P., Mache R., Schlenker M. and Lerbs-Mache S.** (2006) Quantitative phase tomography of Arabidopsis seeds reveals intercellular void network. Proceedings of

the National Academy of Sciences of the United States of America **103:** 14626-14630

**De Veylder L., Beeckman T. and Inze D.** (2007) The ins and outs of the plant cell cycle. Nature Reviews. Molecular Cell biology **8:** 655-665

**Dewitte W., Riou-Khamlichi C., Scofield S., Healy J.M.S., Jacqmard A., Kilby N.J. and Murray J.A.** (2003) Altered cell cycle distribution, hyperplasia, and inhibited differentiation in Arabidopsis caused by the D-type cyclin CYCD3. Plant Cell **15:** 79-92

**Dhondt S., Vanhaeren H., Van Loo D., Cnudde V. and Inze D.** (2010) Plant structure visualization by high-resolution X-ray computed tomography. Trends in Plant Science **15:** 419-422

**Dorca-Fornell C., Pajor R., Lehmeier C., Perez-Bueno M., Bauch M., Sloan J., Osborne C., Rolfe S., Sturrock C., Mooney S. and Fleming A.** (2013) Increased leaf mesophyll porosity following transient retinoblastoma-related protein silencing is revealed by microcomputed tomography imaging and leads to a system-level physiological response to the altered cell division pattern. The Plant Journal **76:** 914-929

**Ethier G.J., Livingston, N.J.** (2004) On the need to incorporate sensitivity to CO2 transfer conductance into the Farquhar-von Caemmerer-Berry leaf photosynthesis model. Plant Cell and Environment **27:** 137-153

**Evans J.R., Santiago, L. S.** (2014) PrometheusWiki Gold Leaf Protocol: gas exchange using LI-COR 6400. Functional Plant Biology **41:** 223-226

**Flexas J., Ribas-Carbo M., Diaz-Espejo A., Galmes J. and Medrano H.** (2008) Mesophyll conductance to CO2: current knowledge and future prospects. Plant, Cell & Environment **31:** 602-621

**Flexas J., Ribas-Carbo M., Diaz-Espejo A., Galmes J. and Medrano H.** (2008) Mesophyll conductance to CO2: current knowledge and future prospects. Plant Cell Environ **31:** 602-621

**Giuliani R., Koteyeva N., Voznesenskaya E., Evans M.A., Cousins A.B. and Edwards G.E.** (2013) Coordination of Leaf Photosynthesis, Transpiration, and Structural Traits in Rice and Wild Relatives (Genus Oryza). Plant Physiol **162:** 1632-1651

**Gowik U., Burscheidt J., Akyildiz M., Schlue U., Koczor M., Streubel M. and Westhoff P.** (2004) cis-Regulatory elements for mesophyll-specific gene expression in the C4 plant Flaveria trinervia, the promoter of the C4 phosphoenolpyruvate carboxylase gene. The Plant Cell **16:** 1077-1090

**Gutzat R., Borghi L. and Gruissem W.** (2012) Emerging roles of RETINOBLASTOMA-RELATED proteins in evolution and plant development. Trends Plant Sci **17:** 139-148

**Hisanaga T., Kawade K. and Tsukaya H.** (2015) Compensation: a key to clarifying the organ-level regulation of lateral organ size in plants. J Exp Bot **66:** 1055-1063

**John G.P., Scoffoni C. and Sack L.** (2013) Allometry of cells and tissues within leaves. American Journal of Botany **100:** 1936-1948

**Kaldenhoff R.** (2012) Mechanisms underlying CO2 diffusion in leaves. Current Opinion in Plant Biology **15:** 276-281

**Kim I., Cho E., Crawford K., Hempel F.D. and Zambryski P.C.** (2005) Cell-to-cell movement of GFP during embryogenesis and early seedling development in *Arabidopsis*. Proc Natl Acad Sci U S A **102:** 2227-2231

**Kuwabara A., Backhaus A., Malinowski R., Bauch M., Hunt L., Nagata T., Monk N., Sanguinetti G. and Fleming A.** (2011) A shift toward smaller cell size via manipulation of cell cycle gene expression acts to smoothen Arabidopsis leaf shape. Plant Physiol **156:** 2196-2206

**Lichtenthaler H.K. and Wellburn A.R.** (1983) Determinations of total carotenoids and chlorophylls a and b of leaf extracts in different solvents. Biochemical Society Transactions **11:** 591-592

**Long S.P. and Bernacchi C.J.** (2003) Gas exchange measurements, what can they tell us about the underlying limitations to photosynthesis? Procedures and sources of error. Journal of Experimental Botany **54:** 2393-2401

**McCann M.C. and Carpita N.C.** (2008) Designing the deconstruction of plant cell walls. Curr Opin Plant Biol **11:** 314-320

**Pajor R., Fleming A., Osborne C.P., Rolfe S.A., Sturrock C.J. and Mooney S.J.** (2013) Seeing space: visualization and quantification of plant leaf structure using X-ray micro-computed tomography: View Point. Journal of Experimental Botany **64:** 385-390

**Parkhurst D.F.** (1994) Diffusion of CO2 and other gases inside leaves. New Phytologist **126:** 449-479

**Rackham O., Wilson, J** (1968) Integrating sphere for spectral measurements on leaves. In The measurement of environmental factors in terrestrial ecology Vol 8. Blackwell

**Terashima I., Hanba Y.T., Tholen D. and Niinemets U.** (2011) Leaf functional anatomy in relation to photosynthesis. Plant Physiol **155:** 108-116

**Valentini R. E.D., De Angelis P., Matteucci G., Dreyer E** (1995) In situ estimation of net CO2 assimilation, photosynthetic electron flow and photorespiration in Turkey oak (Q. cerris L.) leaves: diurnal cycles under different levels of water supply. Plant, Cell & Environment **18:** 631-640

**Verkest A., Manes C.-L., Vercruysse S., Maes S., Van Der Schueren E., Beeckman T., Genschik P., Kuiper M., Inzé D. and De Veylder L.** (2005) The cyclin-dependent kinase inhibitor KRP2 controls the onset of the endoreduplication cycle during Arabidopsis leaf development through inhibition of mitotic CDKA;1 kinase complexes. Plant Cell **17:** 1723-1736

**Verkest A., Weinl C., Inzé D., De Veylder L. and Schnittger A.** (2005) Switching the cell cycle. Kip-related proteins in plant cell cycle control. Plant Physiol **139:** 1099-1106

**von Caemmerer S.** (2013) Steady-state models of photosynthesis. Plant, Cell & Environment **36:** 1617-1630

**von Caemmerer S. and Farquhar G.D.** (1981) Some relationships between the biochemistry of photosynthesis and the gas exchange of leaves. Planta **153:** 376-387

**Weinl C., Marquardt S., Kuijt S.J.H., Nowack M.K., Jakoby M.J., Hülskamp M. and Schnittger A.** (2005) Novel functions of plant cyclin-dependent kinase inhibitors, ICK1/KRP1, can act non-cell-autonomously and inhibit entry into mitosis. Plant Cell **17:** 1704-1722

**Wildwater M., Campilho A., Perez-Perez J.M., Heidstra R., Blilou I., Korthout H., Chatterjee J., Mariconti L., Gruissem W. and Scheres B.** (2005) The *RETINOBLASTOMA-RELATED* gene regulates stem cell maintenance in *Arabidopsis* roots. Cell **123:** 1337-1349

**Yin X. and Struik P.C.** (2009) Theoretical reconsiderations when estimating the mesophyll conductance to CO(2) diffusion in leaves of C(3) plants by analysis of combined gas exchange and chlorophyll fluorescence measurements. Plant, Cell & Environment **32:** 1513-1524

**Zhu X.G., Long S.P. and Ort D.R.** (2010) Improving photosynthetic efficiency for greater yield. Annual Review of Plant Biology **61:** 235-261

## FIGURE LEGENDS

**Fig. 1. Modulation of cell cycle genes leads to changes in leaf cell size, density and porosity. (A)** Palisade cell size **(B)** Palisade cell density and **(C)** Leaf porosity in *Col-0*, $RBCS_{pro}$:KRP1, $ATML1_{pro}$:KRP1 and $CA1_{pro}$:RBRi leaves, as indicated. Values are means, error bars = sem. For A,B, at least 15 cells were imaged per sample, with a total of 12 samples being analysed from three plants (n =12); for C, porosity values were measured in leaf disks taken from six independent plants (n = 6). Samples were compared with ANOVA followed by a post-hoc Tukey test. Columns indicated by identical letters within each analysis cannot be distinguished from each other at the 0.05 confidence limit.

**Fig. 2. MicroCT imaging reveals variation in leaf airspace patterns. (A-D)** 3D rendering of tissue blocks from **(A)** *Col-0*, **(B)** $RBCS_{pro}$:KRP1, **(C)** $ATML1_{pro}$:KRP1 and **(D)** $CA1_{pro}$:RBRi leaf samples. **(E-L)** Paradermal sections through the tissue blocks shown in A-D at a position towards the adaxial palisade surface (E-H) or towards the abaxial spongy surface (I-L). In A-L, solid tissue has been painted green, airspace yellow.

**(M)** porosity values **(N)** air channel diameter **(O)** air channel circularity and **(P)** air channel density at distances below the adaxial surface of samples from WT (black), $RBCS_{pro}$:KRP1 (green), $ATML1_{pro}$:KRP1 (red) and $CA1_{pro}$:RBRi (blue) leaves. For clarity, only mean values are indicated. Resolution in E-L = 2.75 µm with scale bars = 0.5 mm.

**Fig. 3. Modulation of cell cycle gene expression leads to altered $CO_2$ assimilation rates**

**(A)** Light saturated assimilation rate per area in in *Col-0*, $RBCS_{pro}$:KRP1, $ATML1_{pro}$:KRP1 and $CA1_{pro}$:RBRi leaves, as indicated. **(B)** as (A) but normalized for porosity **(C)** palisade mesophyll porosity for *Col-0*, $RBCS_{pro}$:KRP1, $ATML1_{pro}$:KRP1 and $CA1_{pro}$:RBRi leaves **(D)**

as (A) but normalized for mesophyll thickness **(E)** spongy mesophyll porosity for the leaf samples as indicated in D. **(F)** as (A) but normalized for porosity and mesophyll thickness. Values are means, error bars = sem. For A,B,D,F, values were measured in leaves from six independent plants (n=6) except for *Col-0* (n=5). For C,D n = 6. Samples were compared with ANOVA followed by a post-hoc Tukey test. Columns indicated by identical letters within each analysis cannot be distinguished from each other at the 0.05 confidence limit.

**Fig. 4. Evidence that increased carboxylation rate is linked to decreased air channel diameter and increased air channel density**

**(A)** $V_{cmax}$ **(B)** exposed mesophyll area per one-sided epidermal area **(C)** mesophyll conductance, $g_m$ after Square Root transformation to equalize standard deviation **(D)** palisade channel diameter **(E)** palisade channel density in *Col-0*, $RBCS_{pro}$:KRP1, $ATML1_{pro}$:KRP1 and $CA1_{pro}$:RBRi leaves, as indicated. Values are means, error bars = sem. Values were measured in leaves from at least five independent plants (n ≥ 5) except for: A (*Col-0* n=5,); C (*Col-0* n=3). Samples were compared with ANOVA followed by a post-hoc Tukey test. Columns indicated by similar letters within each analysis cannot be distinguished from each other at the 0.05 confidence limit.

**Fig. 5. Analysis of $ATML1_{pro}$:KRP1 leaves reveals an altered air channel network**

**(A)** and **(B)** Images of the skeletonised air channel network in the palisade layer of *Col-0* (A) and $ATML1_{pro}$:KRP1 (B) leaves. **(C)** and **(D)** As in (A, B) but images are of the spongy layer in the respective genotypes, as indicated. The voxels are colour-coded so that: yellow = 2 connections per voxel; green > 2 connections per voxel; magenta < 2 connections per voxel (= network endpoint). **(E)** mean branch length **(F)** branch density **(G)** connection density and **(H)** tortuosity values for the palisade and mesophyll layers from *Col-0* and $ATML1_{pro}$:KRP1 leaves, as indicated. Values are means, error bars = sem. Values were measured in leaves from six independent plants for Col-0; and twelve independent plants for $ATML1_{pro}$:KRP1. Samples were compared with ANOVA followed by a post-hoc Tukey test. Columns indicated by similar letters within each analysis cannot be distinguished from each other at the 0.001 confidence limit (except for in G, WT spongy vs $ATML1_{pro}$:KRP1 spongy, $p < 0.01$).

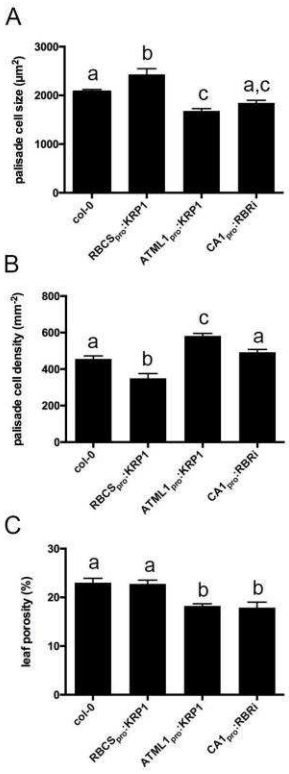


**Fig. 1 Modulation of cell cycle genes leads to changes in leaf cell size, density and porosity. (A)** Palisade cell size **(B)** Palisade cell density and **(C)** Leaf porosity in *Col-0*, RBCS$_{pro}$:KRP1, ATML1$_{pro}$:KRP1 and CA1$_{pro}$:RBRi leaves, as indicated. Values are means, error bars = sem. For A,B, at least 15 cells were imaged per sample, with a total of 12 samples being analysed from three plants (n =12); for C, porosity values were measured in leaf disks taken from six independent plants (n = 6). Samples were compared with ANOVA followed by a post-hoc Tukey test. Columns indicated by identical letters within each analysis cannot be distinguished from each other at the 0.05 confidence limit.

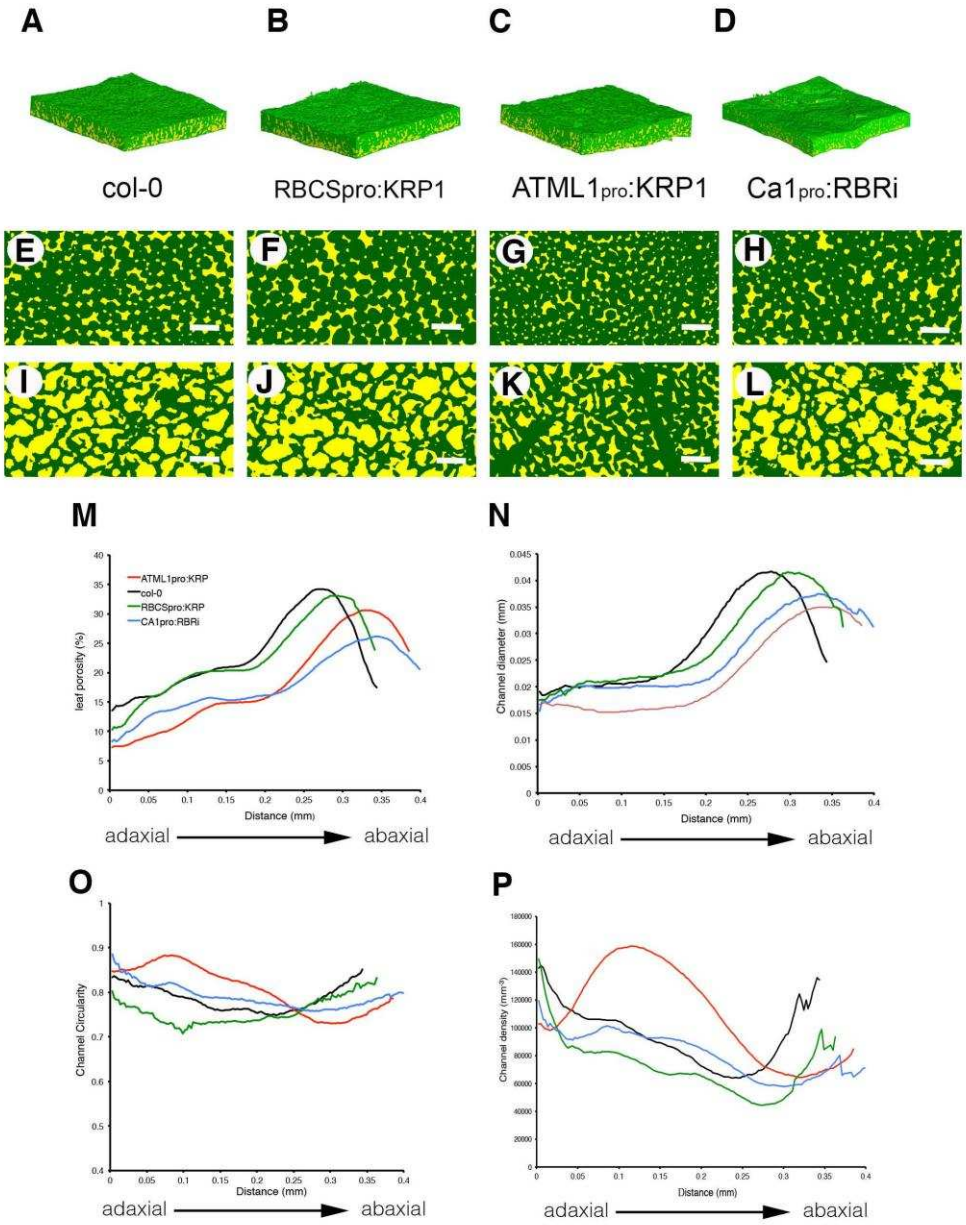

**Fig. 2 MicroCT imaging reveals variation in leaf airspace patterns. (A-D)** 3D rendering of tissue blocks from **(A)** *Col-0*, **(B)** $RBCS_{pro}$:KRP1, **(C)** $ATML1_{pro}$:KRP1Y and **(D)** $CA1_{pro}$:RBRi leaf samples. **(E-L)** Paradermal sections through the tissue blocks shown in A-D at a position towards the adaxial palisade surface (E-H) or towards the abaxial spongy surface (I-L). In A-L, solid tissue has been painted green, airspace yellow.
**(M)** porosity values **(N)** air channel diameter **(O)** air channel circularity and **(P)** air channel density at distances below the adaxial surface of samples from WT (black), $RBCS_{pro}$:KRP1 (green), $ATML1_{pro}$:KRP1 (red) and $CA1_{pro}$:RBRi (blue) leaves. For clarity, only mean values are indicated. Resolution in E-L = 2.75 µm with scale bars = 0.5 mm.

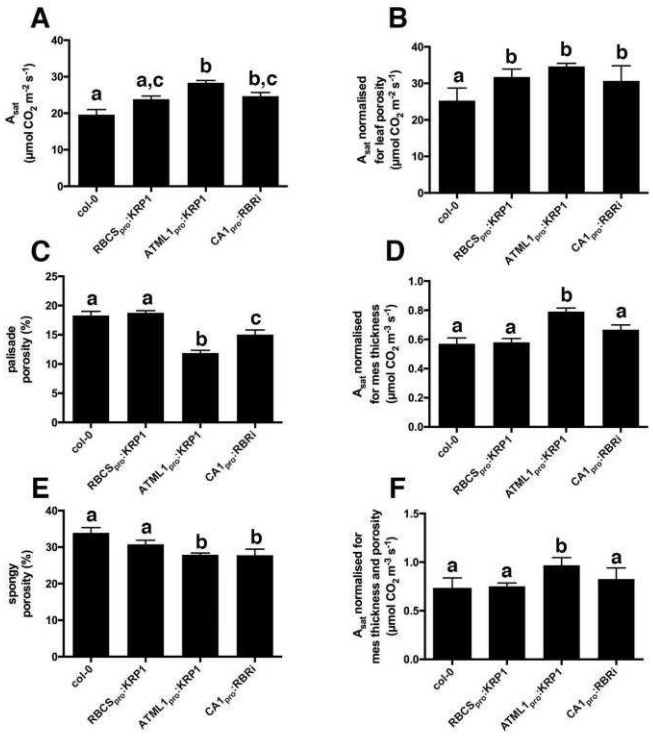


**Fig. 3 Modulation of cell cycle gene expression leads to altered CO2 assimilation rates**

**(A)** Light saturated assimilation rate per area in in *Col-0*, RBCS$_{pro}$:KRP1, ATML1$_{pro}$:KRP1 and CA1$_{pro}$:RBRi leaves, as indicated. **(B)** as (A) but normalized for porosity. **(C)** palisade mesophyll porosity for *Col-0*, RBCS$_{pro}$:KRP1, ATML1$_{pro}$:KRP1 and CA1$_{pro}$:RBRi leaves **(D)** as (A) but normalized for mesophyll thickness **(E)** spongy mesophyll porosity for the leaf samples as indicated in D. **(F)** as (A) but normalized for porosity and mesophyll thickness. Values are means, error bars = sem. For A,B,D,F, values were measured in leaves from six independent plants (n=6) except for *Col-0* (n=5). For C,E (n = 6). Samples were compared with ANOVA followed by a post-hoc Tukey test. Columns indicated by identical letters within each analysis cannot be distinguished from each other at the 0.05 confidence limit.

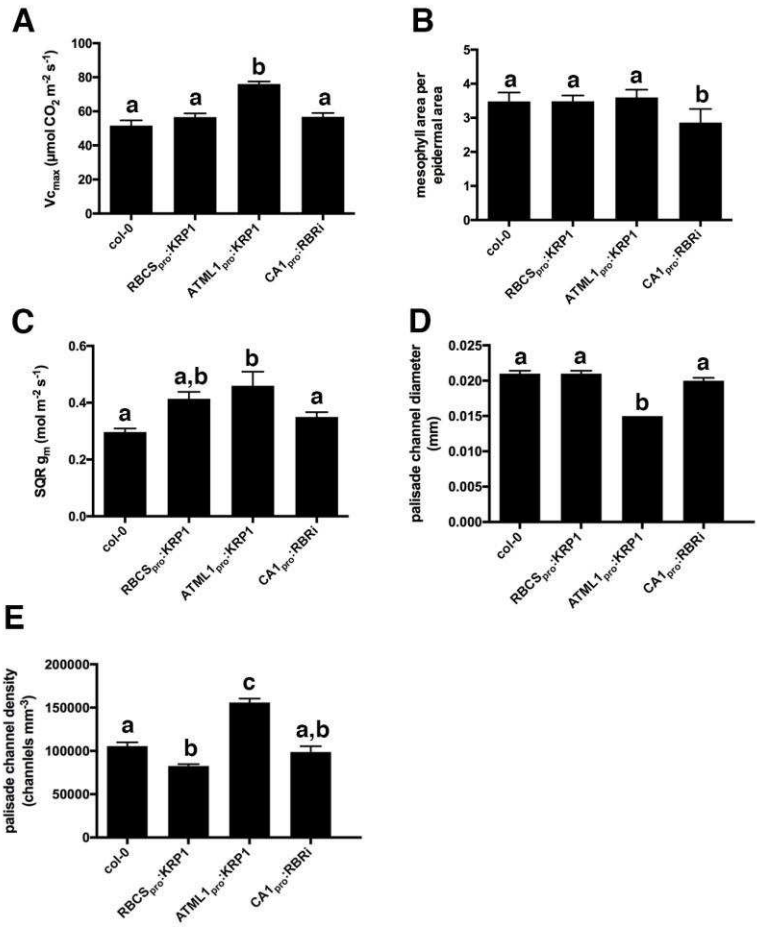

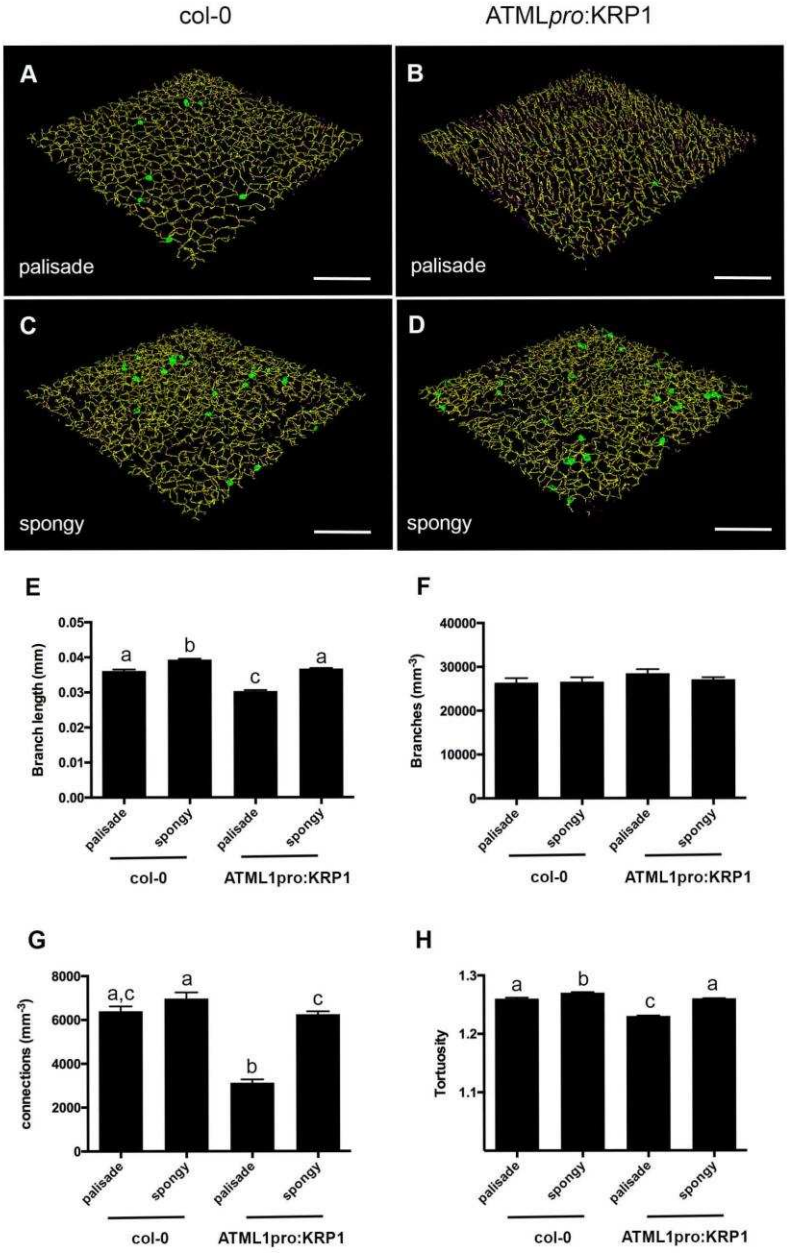


Fig 5

**Fig. 5 Analysis of ATML1$_{pro}$:KRP1 leaves reveals an altered air channel network**

**(A)** and **(B)** Images of the skeletonised air channel network in the palisade layer of *Col-0* (A) and ATML1$_{pro}$:KRP1 (B) leaves. **(C)** and **(D)** As in (A, B) but images are of the spongy layer in the respective genotypes, as indicated. The voxels are colour-coded so that: yellow = 2 connections per voxel; green > 2 connections per voxel; magenta < 2 connections per voxel (= network endpoint). **(E)** mean branch length **(F)** branch density **(G)** connection density and **(H)** tortuosity values for the palisade and mesophyll layers from *Col-0* and ATML1$_{pro}$:KRP1 leaves, as indicated. Values are means, error bars = sem. Values were measured in leaves from six independent plants for Col-0; and twelve independent plants for ATML1$_{pro}$:KRP1. Samples were compared with ANOVA followed by a post-hoc Tukey test. Columns indicated by similar letters within each analysis cannot be distinguished from each other at the 0.001 confidence limit (except for in G, WT spongy vs ATML1$_{pro}$:KRP1 spongy, $p < 0.01$).